ACS Sustainable Chemistry & Engineering

pubs.acs.org/journal/ascecg

Research Article

# Seawater-Powered PEC Photodetectors Based on a Layered Metal Dichalcogenide for Marine Underwater Optical Communication

Preet Deepankumar Vyas,* Devang Dhorada, Kevin Bhanderi, Akshaybhai J. Patel, Shubham Umeshkumar Gupta, Vismay Trivedi, Sanjay A. Bhakhar, Arun Anand, and Kireetkumar Patel*

Cite This: *ACS Sustainable Chem. Eng.* 2025, 13, 12010−12021

Read Online

ACCESS | Metrics & More | Article Recommendations | Supporting Information

**ABSTRACT:** In order to protect the ocean ecosystem, the pursuit of sustainable and self-powered photodetectors is critical for revolutionizing underwater optical communication (UOC) used for environmental hazard sensing. This step enables energy-efficient and real-time detection of marine ecosystem threats such as chemical contamination, oil spill, and eutrophication. Although layered metal dichalcogenides (LMDCs) with exceptional optoelectronic properties and chemical stability are the most suitable materials, their integration into UOC technology remains largely unexplored. To address this, the present study demonstrates and evaluates seawater-immersed photoelectrochemical photodetectors (PEC-PDs) based on $SnSe_2$, an emerging member from the LMDC family. Direct vapor transport-grown $SnSe_2$ is well characterized in its thin-film form by X-ray diffraction, X-ray photoelectron spectroscopy, scanning electron microscopy, atomic force microscopy, Raman spectroscopy, and PL spectroscopy, followed by utilization as photoelectrodes in the PEC-PD devices. Fabricated PEC-PDs exhibit a responsivity of 505.74 ± 4.65 μA/W at zero bias and 10.34 ± 0.16 mA/W at 0.4 V bias; they outperform conventional $Na_2SO_4$-based devices by 21-fold and 82-fold, respectively. To the best of our knowledge, this is the first report presenting an $SnSe_2$-based PEC-PD utilizing seawater electrolyte and its performance evaluation. A proof-of-concept UOC demonstration of the present study paves the way toward the next-generation green optoelectronic devices for self-sustainable marine technologies.

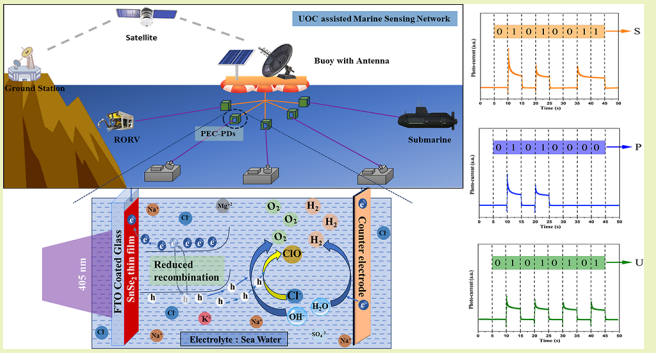


**KEYWORDS:** *self-sustainable, $SnSe_2$, ocean health monitoring, optical links, marine environmental sensing network*



## 1. INTRODUCTION

The development of efficient, cost-effective, and eco-friendly photodetectors remains a significant focus of research, driving exploration toward novel materials and innovative device architectures. To convert optical energy into electrical energy, the photodetector requires an external bias for the separation of charge carriers. In the case of self-powered photodetectors (SP-PDs), this separation is driven by an internal electric field. Out of all the possible architectures of SP-PDs, PEC photodetectors stand out for their simplified fabrication processes, ability to operate effectively in aqueous environments, and potential for self-powered operation.[1] PEC-PDs take advantage of the internal electric field induced between the semiconductor and electrolyte for the separation of charge carriers, resulting in self-powered photodetection.[2] Apart from its application as a photodetector, electrochemical research has the potential to be used for a wide range of sustainable applications like solar cells, dye degradation, carbon dioxide reduction, water splitting, and wastewater treatment.[3−7]

In the search for suitable materials for PEC photodetectors, layered metal dichalcogenides (LMDCs) have garnered substantial attention due to their large specific area and unique layer-dependent optoelectronic and electronic properties.[8−10] Compared to other layered materials like black phosphorus, LMDC materials have better chemical stability.[11] Unlike graphene, these materials have layer-dependent sizable band gaps, making them a better option for switching applications.[12,13] Out of the LMDC family, $SnSe_2$ has emerged as a prime candidate for low and self-powered electronic and optoelectronic sensing applications such as gas sensor, pressure sensor, photo sensor, and humidity sensor due to its fascinating properties like strong light−matter interaction, high conductivity, suitable bandgap, higher intrinsic carrier mobility, appropriate band structure, higher thermoelectricity, and ability to withstand extreme temperature conditions.[14−22]

Received: April 12, 2025
Revised: July 7, 2025
Accepted: July 8, 2025
Published: July 16, 2025

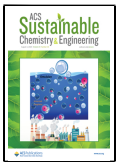

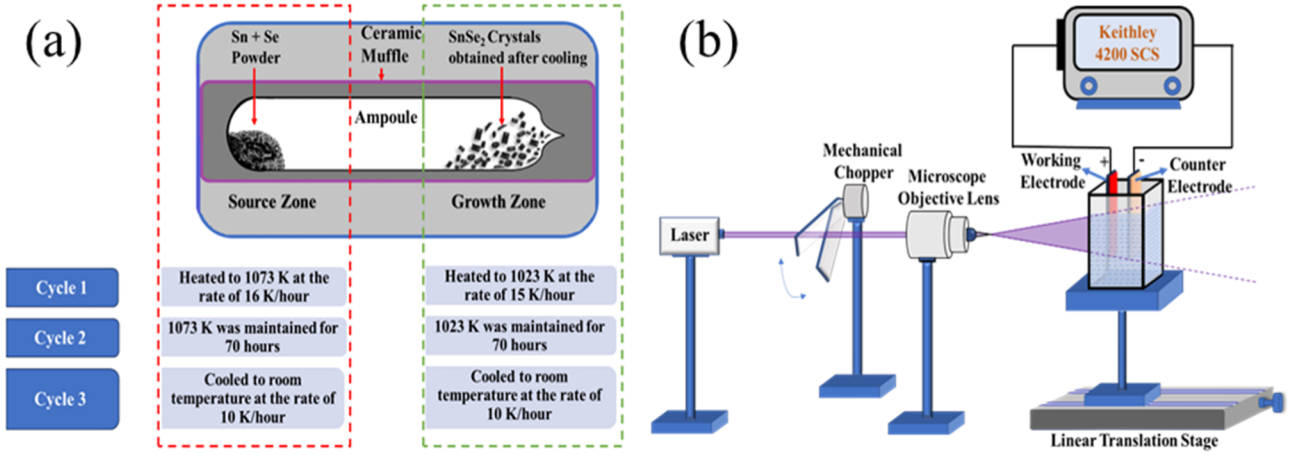


**Figure 1.** (a) Schematic diagram of a dual zone furnace and temperature cycles used for the growth of $SnSe_2$ crystals. (b) Schematic diagram of the experimental setup for the determination of photoresponse characteristics.

$SnSe_2$ possesses a $CdI_2$-type hexagonal lattice structure. It has a layered structure in which one tin atom is strongly bonded to two selenium atoms, forming a sheet of Se−Sn−Se. One sheet of Se−Sn−Se is weakly bonded with another sheet via van der Waals bonds.[22−24] Since Sn and Se are earth-abundant elements, $SnSe_2$ is an affordable material.[25] Due to its lower melting point compared to other LMDC materials like $MoSe_2$, $WSe_2$, and $NbSe_2$, the growth of $SnSe_2$ crystals and thin films requires comparatively low processing temperatures.[23,26−28] These properties make devices based on $SnSe_2$ thin films economical and technologically more feasible for large-scale fabrication. Previous studies have shown that the influence of metal incorporation or chalcogen substitution significantly impacts the material properties and device performance. Shubham et al. demonstrated that Pd incorporation into $SnSe_2$ leads to polymorphic $Pd_XSn_{1-X}Se_2$. In particular, crystals with $X = 0.4$ formed a hexagonal-orthorhombic mix phase and showcased a detectivity of $2.41 \times 10^8$ Jones and responsivity of 0.24 mA/W at an ultralow bias of 10 $\mu$V and a temperature of 10 K.[22] Similarly, Yury et al. reported bandgap tuning of $SnS_{2-X}Se_X$ (where $X = 0$ to 2) nanosheets from 2.23 to 1.29 eV by controlled substitution of Se into $SnS_2$ nanosheets. The photodetectors based on these nanosheets presented an excellent maximum responsivity of 35 mA/W with good stability across the UV and visible range.[29] Furthermore, many similar reports highlight stoichiometry tuning as an effective tool to optimize material properties to enhance the device performance.[30−32]

Different techniques such as chemical vapor deposition,[33,34] molecular beam epitaxy,[35−37] and mechanical exfoliation[38−40] have been used previously to obtain LMDC materials, including $SnSe_2$ with high crystallinity for various electronic and optoelectronic applications. These techniques suffer from drawbacks such as limited area coverage, substrate limitation, small domain size, and expensive instruments.[11,41] This work utilizes physical vapor deposition due to its speed, simplicity, low cost, and ability to produce large area films compared to other methods. This makes our approach particularly suitable for large-area growth and economic production. Furthermore, fabricating a self-powered P−N junction photodetector increases the fabrication steps, resulting in high production cost. Using the Schottky junction to fabricate the photodetector based on $SnSe_2$ is a difficult task because of its higher work function ($\phi$ = 5.3 eV) compared to the conventional metals.[42] As a result, the PEC device architecture emerges as a promising solution for developing self-powered and affordable photodetectors based on $SnSe_2$. While PEC-PDs based on layered materials using conventional electrolytes such as $Na_2SO_4$,[43] $H_2SO_4$,[44] and KOH[11] have been reported, the use of actual seawater as an electrolyte remains largely unexplored. This research gap presents a compelling opportunity to advance the sustainability of LMDC-based photodetectors by harnessing the abundant and eco-friendly resource of seawater as an alternative to conventional electrolytes.

To address this gap, this study evaluates the performance of seawater-immersed $SnSe_2$ PEC-PD under varying incident light power and applied bias conditions. The performance is then compared with the PEC-PD utilizing $Na_2SO_4$ as an electrolyte to determine the influence of the choice of the electrolyte on the efficiency of the device. The PEC-PD device utilizing seawater exhibited an impressive responsivity of $(0.505 \pm 0.004)$ mA/W and a high specific detectivity ($D^*$) of $(9.47 \pm 0.09) \times 10^8$ Jones, without applying an external bias. Furthermore, the photodetector showcased rapid temporal response characteristics with rise and decay times of 45 and 20 ms, respectively. By applying a small bias of 0.4 V, a responsivity as high as $(10.34 \pm 0.16)$ mA/W and a high specific detectivity ($D^*$) of $(38.1 \pm 0.66) \times 10^8$ Jones were achieved. Additionally, this study demonstrated the practical application of this device in optical communication by successfully detecting light pulses encoded with ASCII messages and converting them into photocurrent pulses, which can be decoded to obtain the original message. These exceptional results not only highlight the potential of seawater as an electrolyte in LMDC-based PEC-PDs but also lead to sustainable, high-performance optoelectronic devices suitable for various applications, including marine environmental monitoring and underwater optical communication systems.

## 2. EXPERIMENTAL DETAILS

**2.1. Material Synthesis and Thin Film Deposition.** Selenium (99.99%) and tin (99.99%) elemental powders were procured from Alfa Aesar and used without any further chemical treatments for purification. High-quality $SnSe_2$ crystals were grown by using the direct vapor transport (DVT) technique. In this method, quartz was chosen as the ampule material because it can withstand temperatures as high as 1700 K. The quartz ampule was thoroughly cleaned using HCl and $H_2SO_4$. Once the ampule was cleaned, HF was used to etch the inner surface of one end of the ampule to provide nucleation sites


https://doi.org/10.1021/acssuschemeng.5c03239
ACS Sustainable Chem. Eng. 2025, 13, 12010−12021

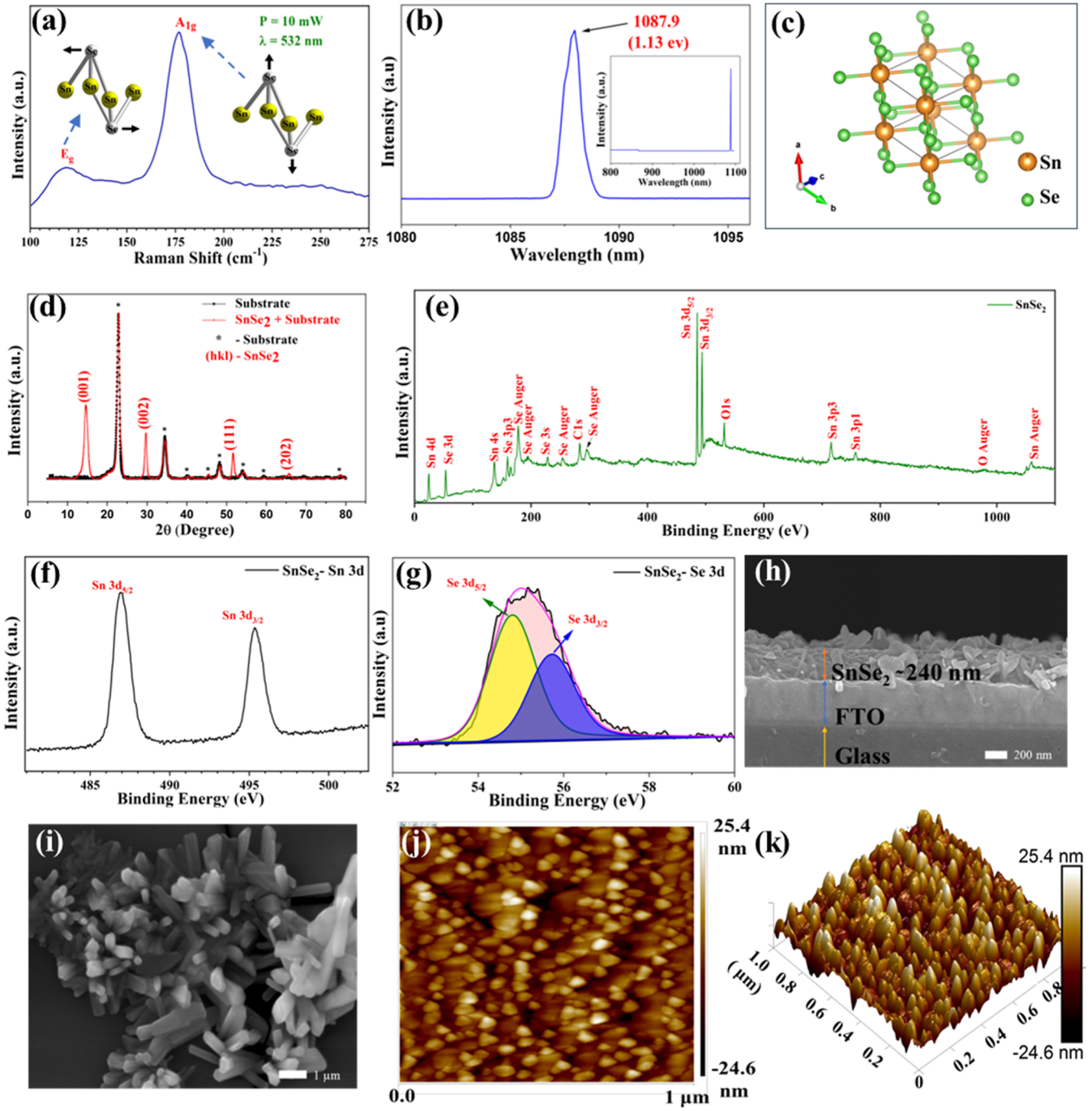


**Figure 2.** (a) Raman spectrum of the $SnSe_2$ thin film along with a schematic illustrating the stretching behavior of Raman active modes in $SnSe_2$. (b) PL spectrum of the $SnSe_2$ thin film. (c) Structural presentation of $SnSe_2$. (d) XRD pattern of the $SnSe_2$ thin film. (e) XPS survey scan spectrum of the $SnSe_2$ thin film. High energy resolution XPS spectra of (f) Sn $3d_{5/2}$ and $3d_{3/2}$ and (g) Se $3d_{5/2}$ and Se $3d_{3/2}$. (h) Cross-sectional and (i) surface FESEM image of the $SnSe_2$ thin film. (j) 2D AFM image and (k) 3D image of the thin film surface.

during the crystal growth. Then it was rinsed with distilled water and heated to 373 K to remove the moisture. After the ampule was completely dried, fine powders of tin (4.29 g) and selenium (5.71 g) were mixed in stoichiometric proportion and inserted inside the quartz ampule. The ampule was evacuated to a vacuum of $10^{-5}$ mbar and sealed off.

Then, the ampule was loaded into the horizontal dual zone high-temperature furnace, as shown in Figure 1a. It consists of two zones: source zone and growth zone. One end of the ampule, which was kept in the source zone, contains the source materials, and the other end having the inner rough surface was kept in the growth zone. Crystals were grown systematically in three steps using the DVT technique. In the first step, the source zone and growth zone were heated to 1073 and 1023 K at a heating rate of 16 K/h and 15 K/h, respectively, to turn the material into its vapor phase. In the following step, the temperature was maintained for 70 h for providing a suitable environment for the source materials to react with each other to form the desired compound material in the vapor phase. During this step, the temperature gradient of 50 K between two zones establishes a vapor pressure gradient between the two zones, which in turn directs the flow of vapor to the growth zone from the source zone. In the final step, the temperature of the source zone and growth zone was cooled down to room temperature at the rate of 10 K/h. As a consequence, shiny crystals were grown at one end of the ampule kept at the growth


https://doi.org/10.1021/acssuschemeng.5c03239
ACS Sustainable Chem. Eng. 2025, 13, 12010−12021

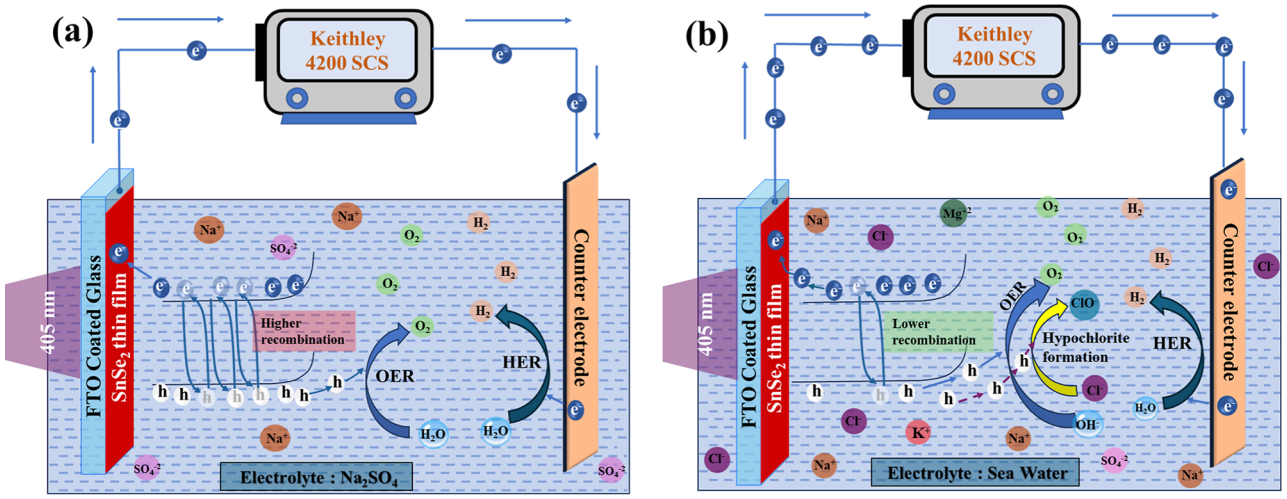


**Figure 3.** Schematic illustration of the working mechanism of PEC-PD based on a $SnSe_2$ thin film employing (a) $Na_2SO_4$ and (b) seawater as an electrolyte.

zone. The grown crystals were crushed using a mortar pestle. The resulting fine powder was used for the deposition of $SnSe_2$ thin films using a Hind High-Vac 12A4D Vacuum Coating Unit. FTO-coated glass slides were purchased from Sigma-Aldrich (transparency ~80%, surface resistivity ~7 Ω/sq) and used as substrates after thorough cleaning using DI water, followed by sonication in acetone. These substrates were dried at 373 K to remove the moisture using the vacuum oven. The thin films were deposited at the rate of 1 Å/s and a vacuum level of $10^{-6}$ mbar to ensure the high quality and uniformity of the thin films. The substrates were kept at 10 cm from the evaporation source, and deposition was carried out, keeping the substrates at room temperature. As-deposited thin films were annealed at a temperature of 423 K in a vacuum of $10^{-1}$ mbar using a vacuum oven and utilized for characterization and PEC-PD application subsequently.

**2.2. Materials Characterizations.** Raman and PL spectra were recorded using the high-resolution Confocal Raman Spectrometer with PL (STR500Airix). Structural confirmation was done by a powder X-ray diffractometer (Bruker) with a radiation source of Cu K$\alpha$ having a wavelength of 1.5418 Å. X-ray photoelectron spectroscopy (XPS) was carried out for elemental confirmation using ESCA+ (Omicron Nanotechnology). JEOL JSM-7600F FEG-SEM was used to investigate surface morphology, and a multimode scanning probe microscope (Bruker) was employed to explore surface topology. UV−visible-NIR absorption spectra were recorded using a Shimadzu UV-2600 spectrophotometer to analyze the optical properties of the thin films.

**2.3. Experimental Setup for Transient Photoresponse.** Experimental arrangement for characterizing the photoresponse of the fabricated PEC-PD is shown in Figure 1b. It consists of a laser source (wavelength = 405 nm, power = 200 mW), mechanical chopper controlled by an Arduino microcontroller, linear translation stage, microscope objective lens (100×, NA = 0.85), and PEC-PD and Keithley 4200 semiconductor characterization system (SCS). To determine the power-dependent photoresponse of a photodetector, it is required to be exposed to different known power levels, and the corresponding response needs to be recorded. One of the ways to obtain different power levels from the same source is to use neutral density filters of different optical densities. However, creating multiple levels of power density requires a large number of neutral density filters or their combinations, which makes it an expensive and cumbersome approach. Another method is to generate a point source from a laser and use the properties of the inverse square law. This law states that for a point source that is capable of radiating omnidirectionally with no obstructions in the vicinity, the intensity $I$ decreases as the square of the distance ($d$) from the source.[45] Mathematically, it can be expressed as

$$I \propto \frac{1}{d^2} \tag{1}$$

Thus, by varying the distance, different power levels can be obtained for determining the power-dependent photoresponse of a photodetector. Moreover, by using a point source kept at a distance, a uniform intensity can be approximated in the region of interest.

Figure 1b demonstrates a schematic experimental setup for the determination of the photoresponse characteristics of the fabricated PEC-PD. In this arrangement, a $SnSe_2$ thin film was used as a working electrode, and a copper plate was used as the counter electrode. Both electrodes were immersed in a chamber containing the electrolyte. A diode laser working at 405 nm was utilized for the excitation of charge carriers. The light was converted into pulses using a mechanical chopper controlled by an Arduino microcontroller. This then passes through a microscope objective lens to create a point source at the back focal plane of the lens, which is then allowed to expand. The PEC-PD was mounted on a linear translation stage, enabling adjustment of the distance between the cell and a point source. By variation of this distance, different power levels were obtained and directed onto the sensitive area of the photodetector. The incident power on the device was calibrated as a function of distance traveled on a linear translation stage using a laser power meter (Thorlabs PM-400).

## 3. RESULTS AND DISCUSSION

The 2H polytype, which is the most common polytype of $SnSe_2$, has three atoms in the unit cell. These results in nine normal modes, including three Raman active modes.[46] In this work, two Raman active modes ($E_g$ and $A_{1g}$) were observed experimentally. The Raman spectrum of the $SnSe_2$ thin film shown in Figure 2a was recorded under the excitation of a 532 nm laser. This figure reveals two significant peaks at 117.3 $cm^{-1}$ and 178 $cm^{-1}$, corresponding to the in-plane $E_g$ and out-of-plane $A_{1g}$ Raman active modes, respectively.[43] The lower frequency $E_g$ mode exhibits in-plane stretching, while high frequency mode $A_{1g}$ is characterized by out-of-plane stretching behavior, as depicted in Figure 2a.[46,47] The inset of Figure 2b depicts PL spectra of the $SnSe_2$ thin film obtained using a 532 nm excitation laser. This spectrum shows a sharp peak at 1087.9 nm (~1.1 eV), which corresponds to the bandgap of the thin film. For better visualization of this peak, an enlarged view of the PL spectrum in the range of 1080−1100 nm is presented in Figure 2b. The narrow fwhm (0.92 nm) of the PL peak suggests a high material purity with minimal defects.



https://doi.org/10.1021/acssuschemeng.5c03239
ACS Sustainable Chem. Eng. 2025, 13, 12010−12021

Analyses of the Raman and PL spectra confirm the high quality of deposited $SnSe_2$ films. The bandgap energy is further confirmed by UV−visible−NIR spectroscopy, as shown in the Supporting Information Figure S1. The Tauc plot presented in Figure S1a indicates a bandgap of approximately 1 eV, while the inset shows an absorbance spectrum. The absorbance spectrum (inset of Figure S1a) and the transmittance spectrum (Figure S1b) together confirm strong a light−matter interaction due to significant optical absorption in the $SnSe_2$ thin film. The crystal structure of $SnSe_2$ is shown in Figure 3c, where it is represented as a layered $CdI_2$-type hexagonal system. Each Sn atom in the structure is octahedrally bound to six Se atoms, thus giving rise to the characteristic Se−Sn−Se sandwich layer. Hexagonal structure and crystalline nature of $SnSe_2$ thin films are confirmed by X-ray diffraction (XRD) patten, as shown in Figure 2d. The XRD spectra of $SnSe_2$ demonstrate typical diffraction peaks at $2\theta$ values of 14.6° and 29.68° corresponding to (001) and (002) planes, respectively. Meanwhile, two relatively weak peaks are observed at 51.64° and 68.78° corresponding to (111) and (202) planes, respectively. A dominant sharp peak detected at 14.6° indicates the (001) plane as the preferred plane of orientation. These diffraction peaks are in good agreement with previously reported data.[28,48] There were no additional peaks observed in XRD spectra, suggesting successful deposition of crystalline $SnSe_2$ thin films having a hexagonal lattice structure. Lattice parameters are found to be $a = b = 3.71$ Å and $c = 6.04$ Å. The unit cell volume was determined to be 71.95 Å$^3$.

The XPS survey scan of $SnSe_2$ thin films was carried out for confirmation of elemental composition and analysis of the bond configuration. Figure 2e illustrates the full spectrum of $SnSe_2$, in which peaks for O are from the FTO substrate and peaks for Sn as well as Se elements are from the $SnSe_2$ thin film. The high energy resolution spectra of Se 3d and Sn 3d were analyzed to confirm the binding state of elements present in the $SnSe_2$ thin film, as displayed in Figure 2f,g, respectively. The symmetrical shape of the Sn 3d energy state shown in Figure 2f indicates the presence of only one valence state of the Sn element. Figure 2f reveals two orbital peaks of Sn 3d belonging to $Sn^{4+}$, located at 486.9 eV ($3d_{5/2}$) and 495.33 eV ($3d_{3/2}$) with an energy difference of 8.43 eV.[49] Figure 2g demonstrates Se 3d energy state deconvoluted into two states Se $3d_{3/2}$ (55.70 eV) and Se $3d_{5/2}$ (54.8 eV) using Gaussian−Lorentz functions. These XPS results are matching with previous reports, further confirming the purity of the deposited $SnSe_2$ thin film.[49,50] Cross-section and surface morphology were analyzed using field emission scanning electron microscopy (FESEM). The thickness of the $SnSe_2$ thin film was determined to be ∼240 nm from the cross-sectional FESEM image, as shown in Figure 2h. Figure 2i shows the presence of randomly oriented rod and platelet-shaped microstructures on the $SnSe_2$ thin film surface, similar to those previously reported by Gupta et al. for $SnSe_2$ thin films.[28] The close packing of these crystallites suggests a high degree of crystallinity and strong film coverage, indicating that the film has a well-formed and uniformly distributed microstructure appropriate for optoelectronic applications. The surface topography of the $SnSe_2$ thin film was analyzed using atomic force microscopy (AFM). Figure 2j demonstrates a 2D AFM image, which reveals a granular surface structure distributed uniformly across the scanned area with minimal defects. The rms roughness of the surface was determined to be 7.64 nm, indicating overall smoothness of the film. The 3D image of the surface was constructed from the height data obtained through a 2D AFM image, as shown in Figure 2k, which provides a detailed representation of the height variation and surface features. A textured surface morphology with peak-to-valley fluctuations ranging from around −24.6 nm to +25.4 nm highlights the nanoscale roughness of the film, which is advantageous for applications like photovoltaic or photodetection systems that need strong light−matter interaction via improved absorption.

The PEC system is used to assess the photodetection properties of the $SnSe_2$ thin film, which also provides insights into its potential for energy harvesting applications. The schematic in Figure 3a,b represents the electrochemistry process involved in the present work, which is responsible for the photoresponsive property and charge transfer mechanism in $SnSe_2$ thin film-based PEC-PDs. In this kind of photodetectors, the substrate acts as a mechanical support for the semiconductor film while serving as the back-contact to collect photogenerated charge carriers and carry them into the external circuit. A good substrate must be chemically stable in the electrolyte, electrically conductive so that it maintains low series resistance, and must be optically transparent to the working spectrum of light. FTO fulfils all these requirements; it is transparent, well over 80% in visible light, has a low sheet resistance, and retains these properties even after high-temperature annealing.[51] Moreover, FTO is very chemically stable in acidic and alkaline environments, which makes it a suitable substrate for PEC-type photodetector applications.[52] The system containing both electrodes is immersed in an aqueous electrolyte solution. When the $SnSe_2$ thin film that exhibits an n-type (confirmed using the hot-probe method) semiconducting nature comes into contact with an electrolyte, electrons are transferred from the semiconductor to the electrolyte to establish electrochemical equilibrium. This transfer causes upward band bending at the $SnSe_2$/electrolyte interface, as shown in Figure 3a,b. This leads to the formation of a space charge region at the interface, resulting in an induced internal electric field. This electric field enables the PEC-PD to work without any external bias.[1,2,42,53] Herein, the $SnSe_2$ thin film serves as the photoelectrode, generating electron−hole pairs ($e^-$−$h^+$) within the material due to its photoactive properties when exposed to light. In the case of a neutral electrolyte like $Na_2SO_4$, due to the built-in electric field at the $SnSe_2$/electrolyte interface, electrons are collected by the FTO and travel toward the counter electrode through the external circuit and take part in hydrogen evolution reaction (HER): $2H_2O + 2e^- = 2OH^- + H_2$. Meanwhile, as a result of upward band bending, photoexcited holes are likely to accumulate at the interface and undergo the oxygen evolution reaction (OER): $2H_2O + 4h^+ = O_2 + 4H^+$.[49,54] A circuit is completed by the counter electrode via its participation in the redox reactions occurring in the ionic channel of the electrolyte. The resultant photocurrent can be measured by using a source measure unit (SMU). When seawater is used as the electrolyte, its slightly alkaline nature modifies the interfacial reactions. During the OER in alkaline media, four holes at the semiconductor surface oxidize hydroxide ions ($OH^-$) into $O_2$, while the HER reaction at the cathode remains same as neutral media. Moreover, because seawater is primarily composed of $Na^+$ and $Cl^-$, chloride ions ($Cl^-$) at the anode are oxidized to form hypochlorite ($ClO^-$) via the reaction: $Cl^- + 2h^+ + 2OH^- = ClO^- + H_2O$.[55] The oxidation of other ionic species present in seawater can be ignored due to


https://doi.org/10.1021/acssuschemeng.5c03239
ACS Sustainable Chem. Eng. 2025, 13, 12010−12021

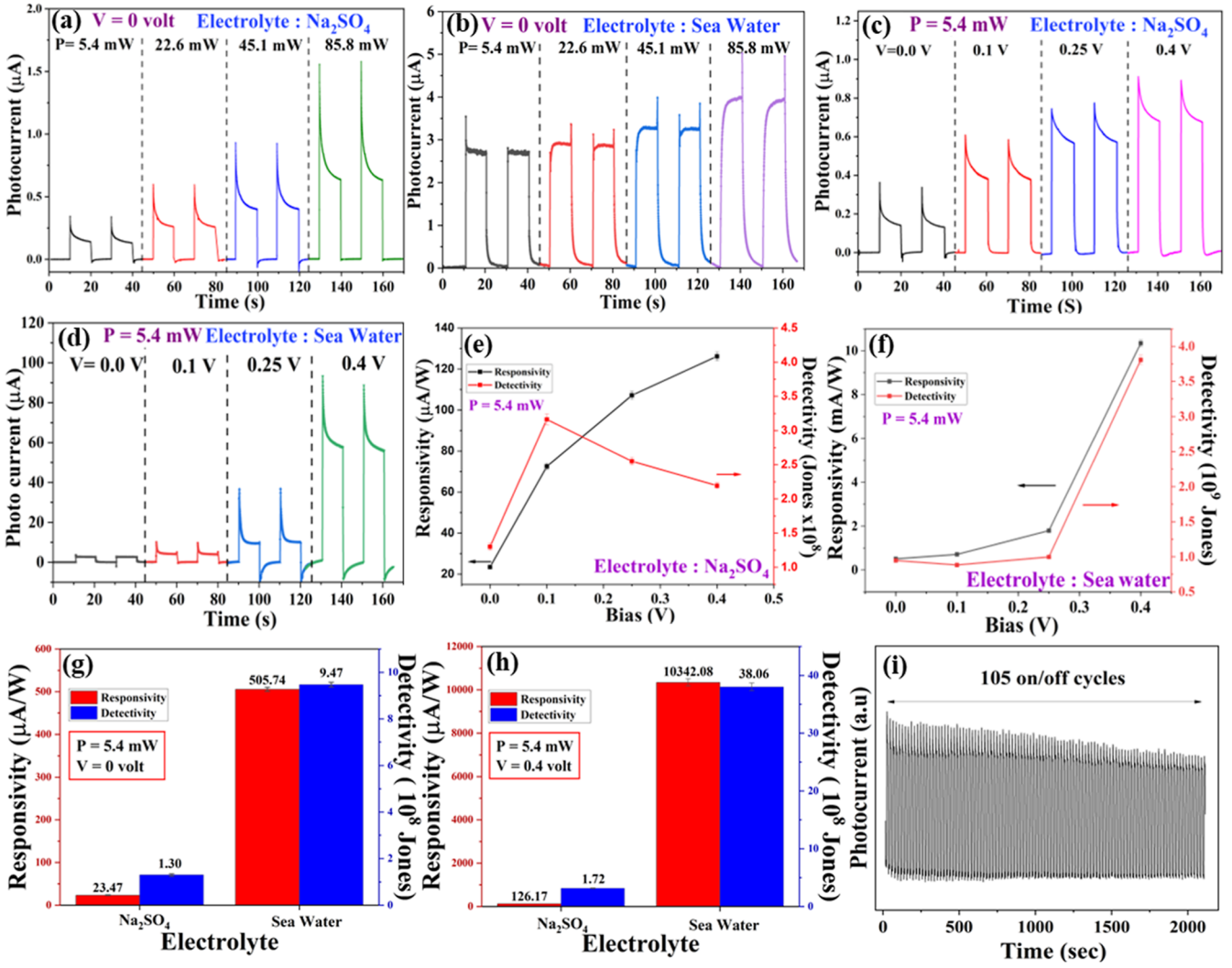


**Figure 4.** Pulsed photoresponse of the PEC-PD under varying incident power densities with (a) $Na_2SO_4$ and (b) seawater as electrolytes. Photoresponse under different applied biases using (c) $Na_2SO_4$ and (d) seawater. Responsivity and detectivity of the PEC-PD as a function of bias when using (e) $Na_2SO_4$ and (f) seawater. Bar diagram comparing responsivity and detectivity for both electrolytes at (g) zero bias and (h) 0.4 V bias. (i) Stability test showing the photocurrent of the self-biased PEC-PD with the seawater electrolyte under 105 on/off cycles for ∼2000 s.

their very low concentration compared to $Cl^-$. OER involves the transfer of $4h^+$, which makes it a kinematically slow process. As a result, holes are accumulated at the interface, leading to a higher recombination rate, as in the case of $Na_2SO_4$, as shown in Figure 3a. Unlike the OER, hypochlorite formation is much faster due to the requirement of just two holes. Due to the high concentration of $Cl^-$ and alkaline nature of seawater, hypochlorite formation competes with the OER at the photoanode and reduces the hole accumulation at the interface. This leads to lower recombination losses, providing seawater with an edge as an electrolyte in PEC systems.

To assess the potential of this PEC-PD, its photodetection characteristics are first evaluated using the conventionally used $Na_2SO_4$ electrolyte, followed by testing with seawater for comparative analysis and its applicability in marine underwater optical communication and sensing networks. The pulsed photoresponse characteristics of the PEC photodetector were analyzed under varying external biases applied to the detector and the power of incident light. To evaluate the pulsed photoresponse characteristics, PEC-PD was exposed to illumination of 10 s from the back of the FTO-coated glass to ensure maximum light reaches the $SnSe_2$ thin film. Figure 4a,b illustrates variation in pulsed photo current under different powers of incident light without any external bias applied to the detector with $Na_2SO_4$ and seawater electrolytes, respectively. Herein, the pulse height increased as the incident power rose from 5.4 to 85.8 mW, demonstrating the power-dependent behavior of the photodetector in both electrolytes. One characteristic of the photoresponse that stands out is the overshooting of current that occurs when light strikes the PEC-PD. This initial current spike, previously reported in PEC-PD devices, is well explained in the literature and is mainly attributed to the surge of carriers.[56] The subsequent decay is caused by fast surface recombination due to the presence of defects.[50,57−60] Here, the photocurrent ($I_{photo}$) is determined as $I_{photo} = I_{light} - I_{dark}$. Here, $I_{light}$ is the current of the PEC-PD when light is switched on, and $I_{dark}$ is the current when the light is turned off. Herein, the photocurrent is found to be enhanced upon increasing incident power. The number of photons striking the material increases with increment in the incident power, which leads to more absorption of photons by the $SnSe_2$ thin film and hence generation of a greater number of electron−hole pairs. These additional carriers contribute to a higher photocurrent. Moreover, enhancement in the carrier


https://doi.org/10.1021/acssuschemeng.5c03239
ACS Sustainable Chem. Eng. 2025, 13, 12010−12021

**Table 1. Performance Comparison of a Previously Reported PEC-Type Photodetector Based on 2D Layered Materials with the Present Study**

| no | materials | method | illumination used | intensity ($mW/cm^2$) | bias | electrolyte | responsivity ($\mu A/W$) | rise time/decay time (ms) | references |
|---|---|---|---|---|---|---|---|---|---|
| 1 | $SnSe_2$ nanosheets | liquid phase exfoliation (LPE) | white LED | 100 | 0 | 0.5 M $Na_2SO_4$ | 1.3 | 400/800 | 43 |
| 2 | $SnSe/SnSe_2$ | physical vapor deposition | simulated light (SL) | 100 | 0.4 | 0.5 M $Na_2SO_4$ | 597 | 13/14 | 49 |
| 3 | InSe nanosheets | LPE | SL | 100 | 1 | 0.2 M KOH | 3.3 | 7000/7000 | 70 |
| 4 | SnS | physical vapor deposition | SL | 100 | 0 | 0.5 M $Na_2SO_4$ | 6.3 | 600/320 | 71 |
| 5 | $Sb_2Te_2Se$ | LPE | 380 nm | 0.32 | 0.6 | 1 M KOH | 744.17 | ~200/~200 | 72 |
| 6 | $Nb_2C$ MXene | HF etching + tetrapropylammonium hydroxide-assisted delamination | 400 nm | 5.22 | 0.6 | 1 M KOH | 3.7 | 150/100 | 73 |
| 7 | $SnSe_2$ | DVT, physical vapor deposition | 405 nm | 8.4 | 0 | 0.5 M $Na_2SO_4$ | 23.4 | 45/27 | present work |
| 8 | $SnSe_2$ | DVT, physical vapor deposition | 405 nm | 8.4 | 0.4 | 0.5 M $Na_2SO_4$ | 126.1 | 34/27 | present work |
| 9 | $SnSe_2$ | DVT, physical vapor deposition | 405 nm | 8.4 | 0 | seawater | 505.7 | 45/20 | present work |
| 10 | $SnSe_2$ | DVT, physical vapor deposition | 405 nm | 8.4 | 0.4 | seawater | 10,342 | 90/180 | present work |

concentration at a higher power can mitigate the space charge effect and improve charge transport, which results in an upsurge in photocurrent. The photocurrent obtained for seawater is about 3.83 $\mu$A, which is approximately 6 times higher than that obtained for $Na_2SO_4$ at a power of 85.1 mW. It is widely known that photodetectors are highly sensitive to applied bias. The photocurrent is also noticed to be increased with the applied external bias while keeping the incident power constant at 5.4 mW with both the electrolyte, as shown in Figure 4c,d. Herein, the built-in electric field at the $SnSe_2$/$Na_2SO_4$ interface promotes the separation of photogenerated electron−hole pairs and allows the device to operate effectively without an external bias. The photocurrent tends to attain the maximum value with increasing bias up to 0.4 V, suggesting enhanced carrier separation under higher electric fields. Since applied bias decreases the recombination of light-induced charge carriers, photocurrent has been found to be increased in both the cases. However, the photocurrent obtained for seawater is about 56.05 $\mu$A, which is significantly higher than that obtained with $Na_2SO_4$ under the identical applied bias condition of 0.4 V.

Responsivity as well as detectivity are paramount in characterizing photodetectors to define the performance of the device and are determined using the following equations[23,61,62]

$$R = I_{photo}/(pS) \tag{2}$$

$$D = R^* \sqrt{\frac{S}{2qI_{dark}}} \tag{3}$$

where $S$ = sensitive area of the PEC-PD (0.64 $cm^2$ in the present work), $p$ = incident power density and $q$ = charge of the electron.

Figure 4e,f depicts variation in responsivity and detectivity with applied bias for PEC-PD using $Na_2SO_4$ and seawater as electrolytes, respectively. In both cases, it was observed that responsivity increases with the applied bias because applied bias acts in harmony with the internal electric field, leading to more effective separation of electron−hole pairs and consequently reducing the recombination rate. As an outcome of increasing bias, the dark current also increases. Since detectivity is proportional to responsivity ($R$) and inversely proportional to dark current ($I_{dark}$), the synergetic effect of both the parameters determines the variation in detectivity ($D$). In the case of the $Na_2SO_4$ electrolyte, the detectivity of PEC-PD increases up to 0.1 V initially, which demonstrates a saturation by reaching its maximum value of about $3.16 \times 10^8$ Jones, followed by a reduction at a higher bias. However, detectivity rises sharply with applied bias and achieves its maximum value of about $3.81 \times 10^9$ Jones at 0.4 V in the case of seawater electrolyte. The power-dependent responsivity and detectivity for PEC-PDs using $Na_2SO_4$ and seawater electrolytes are presented in Figure S2. In both cases, responsivity and detectivity were found to decrease with an increase in incident power. This could be due to the fact that a higher number of photo-induced carriers are generated at higher power, which in turn increases the probability of recombination.[63] Additionally, at elevated power levels, the device may go under self-heating, further increasing recombination.[64] As the recombination rate increases, fewer carriers contribute to photocurrent, leading to a reduction in both responsivity and detectivity at higher power levels. Figure 4g,h presents a comparative analysis of responsivity and detectivity of PEC-PD for $Na_2SO_4$ and seawater as electrolytes through bar diagrams. Figure 4g presents the comparison at zero bias, in which responsivity portrayed by PEC-PD is much lower of about 23.47 $\mu$A/W in $Na_2SO_4$, and it reaches 505.74 $\mu$A/W in seawater, which is significantly greater compared to that of $Na_2SO_4$. Seawater-immersed PEC-PD also demonstrated a significantly higher detectivity of $9.47 \times 10^8$ Jones in a comparison with the $Na_2SO_4$ immersed system. Similarly, at the applied bias of 0.4 V, as illustrated in Figure 4h, the responsivity of PEC-PD in seawater exhibited a dramatic rise to 10.33 mA/W, which is approximately 82 times higher than that in $Na_2SO_4$. Additionally, PEC-PD utilizing seawater far outperforms the one with $Na_2SO_4$ by displaying a remarkable detectivity of about $3.81 \times 10^9$ Jones, which reflects its exceptional photo sensing capabilities even at the low applied bias of 0.4 V. These outcomes suggest that the PEC-PD in seawater exhibits strong sensitivity and the capability to detect weak signals both in self-biased and externally biased operating conditions. Herein, it is


https://doi.org/10.1021/acssuschemeng.5c03239
ACS Sustainable Chem. Eng. 2025, 13, 12010−12021

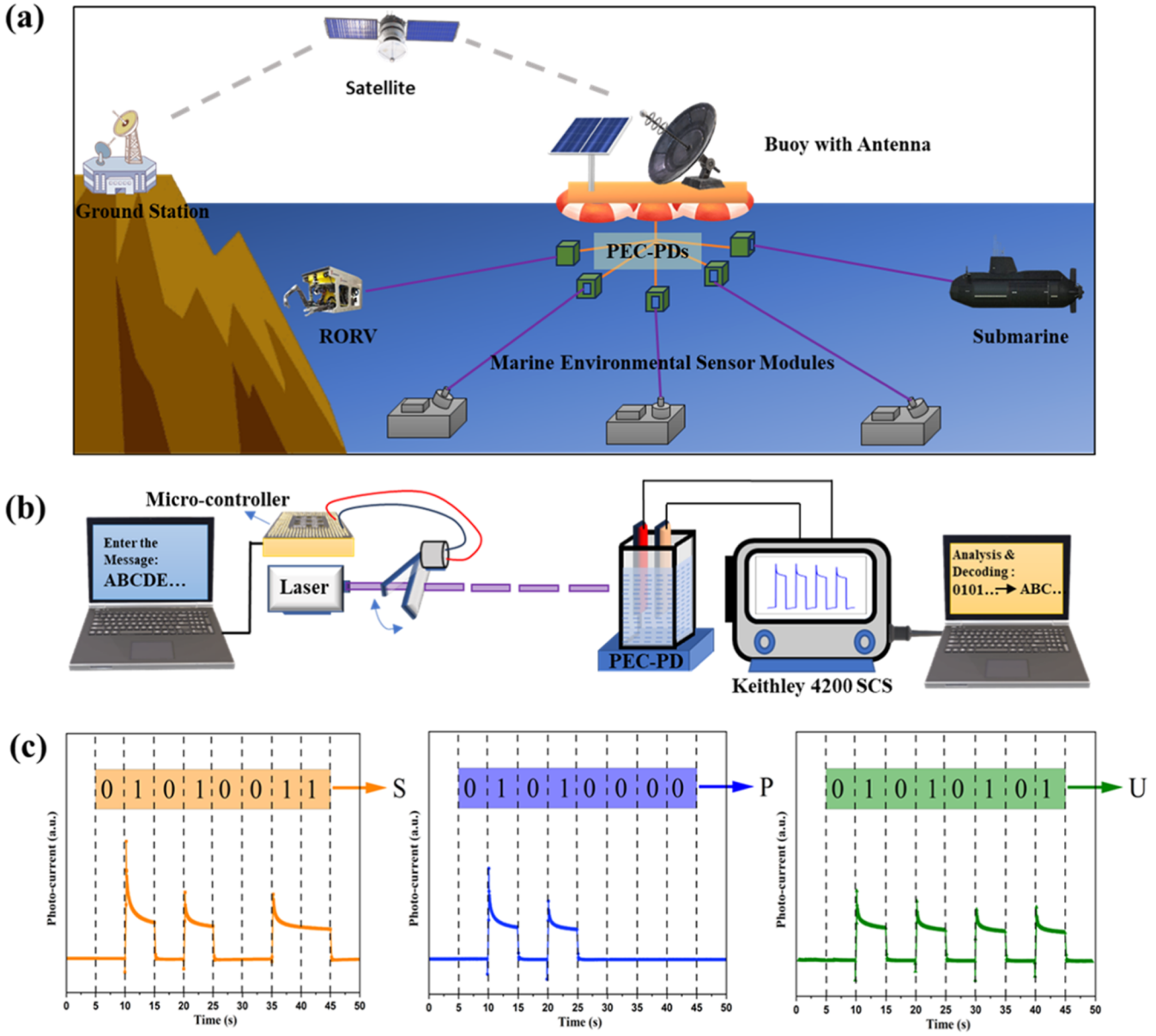


**Figure 5.** (a) Schematic diagram showing the potential application of $SnSe_2$-based PEC-PD for marine environmental monitoring. (B) Experimental setup mimicking the underwater data transmission. (C) Binary current pulses generated by the PEC-PD and the corresponding digital message.

observed that PEC-PD in the seawater electrolyte showcases enhanced noise resistance and a superior capability of detecting weak signals compared to PEC-PD with $Na_2SO_4$. Along with responsivity and detectivity, rise time and decay time of the photodetector are the crucial parameters that need to be determined. The rise time of a photodetector is defined as the time required to reach the 90% value of photocurrent from its 10% value. In a similar manner, decay time is defined as the time required to drop to 10% of the photocurrent from 90% of its value. At the zero applied bias, PEC-PD based on $SnSe_2$ with seawater as an electrolyte showcased a quick rise time of 45 ms and decay time of 20 ms. Figure 4i demonstrates the stability of the PEC-PD using the seawater electrolyte under 105 continuous periodic illumination on/off cycles over approximately 2000 s, demonstrating excellent operational stability with negligible change in steady-state photocurrent. High responsivity and detectivity, along with fast response time and good stability, achieved using seawater, make the $SnSe_2$-based PEC-PD a prime candidate for marine underwater optical communication and sensing networks. Table 1 shows a comparison of this PEC-PD with that of the previously reported photodetectors.

The noteworthy variation in performance underscores the benefit of seawater's increased electrochemical activity and ionic conductivity in promoting effective charge carrier generation as well as separation. The results of the present investigation highlight the importance of electrolyte selection to enhance PEC-PD performance. Herein, seawater is emphasized as a more efficient electrolyte as compared to the conventionally used $Na_2SO_4$. The high performance of PEC-PD observed in the seawater electrolyte compared with that of $Na_2SO_4$ can be attributed to several factors. Apart from NaCl, seawater contains a variety of dissolved salts, resulting in the presence of various ionic species such as magnesium


https://doi.org/10.1021/acssuschemeng.5c03239
ACS Sustainable Chem. Eng. 2025, 13, 12010−12021

($Mg^{2+}$), calcium ($Ca^{2+}$), potassium ($K^+$), and sulfate ($SO_4^{2-}$). This leads to a larger concentration and variety of charge carriers, in contrast to $Na_2SO_4$. These ions contribute to a higher ionic conductivity of seawater and promote better charge transport channels within the electrolyte by lowering resistance and boosting the total photocurrent.[65] Similarly, Zhang et al. showed that the $Na^+$ and $Cl^-$ in seawater enhance the conductivity and accelerate the redox reaction at the electrode interface.[66] The presence of a variety of charge carriers not only contributes to ionic conductivity but also stabilizes the photocurrent generation by effectively suppressing the Coulombic attraction between the electron−hole pair and contributes to enhanced photocurrent. According to Li et al., seawater ions get adsorbed onto oppositely charged facets of the photoelectrode, leading to a significant increase in carrier lifetime.[67] Due to this, holes and electrons remain apart for a longer time, resulting in a lower recombination rate. Meanwhile, $Na_2SO_4$ solution operates with less ionic strength, thereby less charge screening and higher recombination rates compared to those in seawater. Furthermore, Iguchi et al. proposed that adding $Cl^-$ is one of the most effective ways for obtaining a hole scavenger in aqueous photochemistry.[68] These ions act as hole scavengers by providing an alternate path to the OER for hole consumption, thereby mitigating hole accumulation at the interface.[69] This improved charge separation ultimately leads to an enhanced photocurrent. Meanwhile, $SO_4^{2-}$ ions in $Na_2SO_4$ are passive ionic species and do not engage in such reactions, leading to hole accumulation and higher recombination losses. Thus, the constituent ionic species of seawater provide a better conduction channel for charge transport, scavenge holes for efficient charge transfer, and create suitable conditions that reduce recombination losses and increase photocurrent generation. This not only enables underwater optical communication but also establishes seawater as a superior choice over the conventionally used $Na_2SO_4$ electrolyte.

Figure 5a illustrates the schematic representation of proof of concept for functioning of $SnSe_2$ PEC-PD in the potential applications of self-powered marine environmental monitoring devices through integration with various sensor nodes consisting of chemical, physical, biological sensors, remote operated research vehicles (RORV), and submarines. In such systems, the data or messages transmitted by these nodes can be intercepted by self-powered PEC-PDs and generated current pulses can be measured by a portable workstation system present on the floating buoy. These data can be transmitted to the ground station via a solar-powered antenna, where it can be decoded to obtain the digital data. Figure 5b shows the experimental setup used to mimic this data transmission process to showcase the potential of the $SnSe_2$-based PEC-PDs for self-powered and wireless underwater data transmission in a marine environment. As depicted in this schematic, messages entered by a user or data obtained from the sensors are converted into binary codes using extended ASCII schemes, which are subsequently transmitted to an Arduino controller-assisted mechanical chopper that chops the light accordingly for conversion of data into pulsed radiation. This pulsed radiation is detected by the $SnSe_2$-based PEC-PD utilizing seawater as an electrolyte, generating the corresponding ASCII-coded current pulses. These current pulses are analyzed and decoded to obtain the original digital message with the help of an indigenously developed Python-based graphical user interface (GUI). Figure 5c shows the binary current pulse generated by the PEC-PD without external bias in response to the incident light pulses. These binary pulses accurately match the binary ASCII code of the digital message sent by the user. Herein, the characters "SPU" were transmitted wirelessly and decoded to obtain the digital message, which serves as a proof of concept for practical and robust application of $SnSe_2$-based PEC-PD for data acquisition as well as real-time monitoring in marine underwater optical communication and sensing networks.

Overall, $SnSe_2$-based PEC-PD displayed impressive performance in seawater compared to $Na_2SO_4$, which indicates its potential for sustainable optoelectronic applications. The inherent nature of seawater enables superior ionic conductivity and carrier transport, which is responsible for this enhancement. Additionally, it is economically advantageous for a device to work at self-bias conditions in seawater, portraying $SnSe_2$ PEC-PD's capacity for an ecologically acceptable and economically viable platform for optical communication under water.

## 4. CONCLUSION

This study demonstrates seawater-powered highly efficient PEC-PD based on a thermally evaporated $SnSe_2$ thin film. A DVT-grown $SnSe_2$ compound is converted into a well-characterized thin film, which exhibits a layered hexagonal structure. This film is utilized as a working electrode to explore the photoresponse of the $SnSe_2$ thin film, in which PEC-PD achieved noteworthy results, demonstrating a high responsivity of $(0.505 \pm 0.004)$ mA/W and detectivity of $(9.47 \pm 0.09) \times 10^8$ Jones at self-bias in seawater. Seawater's better ionic conductivity is responsible for the augmented photoresponse of PEC-PD. The device performance is further improved upon applying a small bias of 0.4 V and exhibits a high responsivity of $(10.34 \pm 0.16)$ mA/W and detectivity of $(3.81 \pm 0.06) \times 10^9$ Jones. This PEC-PD also displayed a rapid response time of about 45 ms rise time and 20 ms decay time. These results are far superior to those obtained for the same device with the conventional $Na_2SO_4$-based PEC-PD. The combined effect of seawater's higher ionic conductivity, redox active species, and pH stability creates a suitable environment for efficient charge transfer and generation of large photocurrent in contrast to $Na_2SO_4$. To validate the potential of technology transfer, a concept validation of underwater optical communication is conducted, in which $SnSe_2$ PEC-PD immersed in seawater successfully decoded the message sent via encoded optical pulses of the word "SPU". This pioneering work showcases the potential of seawater-powered $SnSe_2$ PEC-PD for advancing the field by rapid as well as high photoresponse, paving the way to revolutionize future underwater optical communication technology.

## ■ ASSOCIATED CONTENT

### Supporting Information

The Supporting Information is available free of charge at https://pubs.acs.org/doi/10.1021/acssuschemeng.5c03239.

UV−visible−NIR spectroscopy of the $SnSe_2$ thin film And power-dependent responsivity and detectivity of PEC-PD based on $SnSe_2$ (PDF)



https://doi.org/10.1021/acssuschemeng.5c03239
ACS Sustainable Chem. Eng. 2025, 13, 12010−12021

## AUTHOR INFORMATION


### Corresponding Authors

**Preet Deepankumar Vyas** − *Department of Physics, Sardar Patel University, Vallabh Vidyanagar, Gujarat 388120, India*; orcid.org/0000-0001-5578-1607; Email: pdvyas33@gmail.com

**Kireetkumar Patel** − *Department of Physics, Sardar Patel University, Vallabh Vidyanagar, Gujarat 388120, India*; Email: kdpatel-phy@spuvvn.edu

### Authors

**Devang Dhorada** − *Department of Physics, Sardar Patel University, Vallabh Vidyanagar, Gujarat 388120, India*

**Kevin Bhanderi** − *Department of Physics, Sardar Patel University, Vallabh Vidyanagar, Gujarat 388120, India*

**Akshaybhai J. Patel** − *L.C. Institute of Technology, Bhandu, Gujarat 384120, India*

**Shubham Umeshkumar Gupta** − *Photoelectric and Energy Device Application Lab (PEDAL), Department of Electrical Engineering, Incheon National University, Incheon 22012, Republic of Korea*; orcid.org/0000-0002-8112-339X

**Vismay Trivedi** − *Department of Aerospace Structures and Materials, Delft University of Technology, 2629 HS Delft, The Netherlands*; orcid.org/0009-0002-7792-7990

**Sanjay A. Bhakhar** − *P.D. Patel Institute of Applied Sciences, Charotar University of Science and Technology, Changa, Gujarat 388120, India*

**Arun Anand** − *Department of Physics, Sardar Patel University, Vallabh Vidyanagar, Gujarat 388120, India*

Complete contact information is available at: https://pubs.acs.org/10.1021/acssuschemeng.5c03239


### Notes

The authors declare no competing financial interest.

## ACKNOWLEDGMENTS

The authors P.D.V., D.D., and K.B. are thankful to the Education Department, Government of Gujarat, for providing financial assistance under the SHODH Scheme. The authors are also thankful to MRC, MNIT Jaipur, for XPS and Raman Spectroscopy and to SAIF, IIT Bombay, for FESEM imaging.

## REFERENCES


(1) Kaur, M.; Kumar, P.; Ghotra, H. S. A Review on Advances in Photoelectrochemical (PEC-Type) Photodetectors: A Trending Thrust Research Area. *Int. J. Hydrogen Energy* **2024**, *49*, 1095−1112.

(2) Wang, D.; Huang, C.; Liu, X.; Zhang, H.; Yu, H.; Fang, S.; Ooi, B. S.; Mi, Z.; He, J. H.; Sun, H. Highly Uniform, Self-Assembled AlGaN Nanowires for Self-Powered Solar-Blind Photodetector with Fast-Response Speed and High Responsivity. *Adv. Opt. Mater.* **2021**, *9* (4), 2000893.

(3) Zhang, Y.; Luc, W.; Hutchings, G. S.; Jiao, F. Photoelectrochemical Carbon Dioxide Reduction Using a Nanoporous Ag Cathode. *ACS Appl. Mater. Interfaces* **2016**, *8* (37), 24652−24658.

(4) Ma, H.; Xiaohui, L.; Luo, X.; Sun, D.; Wang, G.; Fu, Y. Constructing Core-Shell Structured Co3O4-MnWO4 Composite Photoelectrode with Superior PEC Water Purification Performance. *Chemosphere* **2024**, *354*, 141648.

(5) Bimli, S.; Mulani, S. R.; Choudhary, E.; Manjunath, V.; Shinde, P.; Jadkar, S. R.; Devan, R. S. Perovskite BaSnO3 Nanoparticles for Solar-Driven Bi-Functional Photocatalytic Activity: PEC Water Splitting and Wastewater Treatment. *Int. J. Hydrogen Energy* **2024**, *51*, 1497−1507.

(6) Suryavanshi, K. E.; Dhake, R. B.; Patil, A. M.; Sonawane, M. R. Growth Mechanism and Transport Properties of Chemically Deposited PbxCd1-XS Thin Film's Photoelectrochemical (PEC) Solar Cell. *Optik* **2020**, *218*, 165008.

(7) Chen, X.; Cao, J.; Chen, C.; Chen, A.; Zheng, W. Degradation of Organic Dyes with Solar PEC Cells Based on Bi2S3/BiVO4/TiO2 Photoanode. *Inorg. Chem. Commun.* **2024**, *160*, 111849.

(8) Zarei, S.; Hosseini, Z.; Sabetghadam, S. A.; Ghanbari, T. Improved Sensitivity in Self-Powered Photoelectrochemical UV Photodetector by Application of Graphene Quantum Dots. *Eur. Phys. J. Plus* **2021**, *136* (5), 515.

(9) Patel, K.; Chauhan, P.; Patel, A. B.; Solanki, G. K.; Patel, K. D.; Pathak, V. M. Orthorhombic SnSe Nanocrystals for Visible-Light Photodetectors. *ACS Appl. Nano Mater.* **2020**, *3* (11), 11143−11151.

(10) Gnanasekar, P.; Periyanagounder, D.; Varadhan, P.; He, J.-H.; Kulandaivel, J. Highly Efficient and Stable Photoelectrochemical Hydrogen Evolution with 2D-NbS2/Si Nanowire Heterojunction. *ACS Appl. Mater. Interfaces* **2019**, *11* (47), 44179−44185.

(11) Chauhan, P.; Patel, A. B.; Solanki, G. K.; Machhi, H. K.; Soni, S. S.; Pathak, V. M.; Patel, V.; Narayan, S.; Jha, P. K. Flexible Self-Powered Electrochemical Photodetector Functionalized by Multilayered Tantalum Diselenide Nanocrystals. *Adv. Opt. Mater.* **2021**, *9* (22), 2100993.

(12) Englert, J. M.; Dotzer, C.; Yang, G.; Schmid, M.; Papp, C.; Gottfried, J. M.; Steinrück, H. P.; Spiecker, E.; Hauke, F.; Hirsch, A. Covalent Bulk Functionalization of Graphene. *Nat. Chem.* **2011**, *3*, 279−286.

(13) Nandee, R.; Chowdhury, M. A.; Shahid, A.; Hossain, N.; Rana, M. Band Gap Formation of 2D Materialin Graphene: Future Prospect and Challenges. *Results Eng.* **2022**, *15*, 100474.

(14) Pallecchi, I.; Caglieris, F.; Ceccardi, M.; Manca, N.; Marré, D.; Repetto, L.; Schott, M.; Bilc, D. I.; Chaitoglou, S.; Dimoulas, A.; Verstraete, M. J. Investigation and Field Effect Tuning of Thermoelectric Properties of SnSe2 Flakes. *Phys. Rev. Mater.* **2023**, *7* (5), 54004.

(15) Li, W.; He, K.; Zhang, D.; Li, N.; Hou, Y.; Cheng, G.; Li, W.; Sui, F.; Dai, Y.; Luo, H.; Feng, Y.; Wei, L.; Li, W.; Zhong, G.; Chen, M.; Yang, C. Flexible and High Performance Piezoresistive Pressure Sensors Based on Hierarchical Flower-Shaped SnSe2 Nanoplates. *ACS Appl. Energy Mater.* **2019**, *2* (4), 2803−2809.

(16) Zankat, C. K.; Pataniya, P. M.; Patel, A.; Bhakhar, S. A.; Narayan, S.; Solanki, G. K.; Patel, K. D.; Pathak, V. M.; Sumesh, C. K.; Jha, P. K. Self-Powered Photodetector Based on SnSe2/MoSe2 Heterostructure. *Mater. Today Energy* **2020**, *18*, 100550.

(17) Chen, Z.; Xiong, L.; Li, G.; Wei, L.; Yang, C.; Chen, M. Wafer-Scale Growth of Vertical-Structured SnSe2 Nanosheets for Highly Sensitive, Fast-Response UV-Vis-NIR Broadband Photodetectors. *Adv. Opt. Mater.* **2022**, *10* (5), 2102250.

(18) Zhou, M.; Chen, X.; Li, M.; Du, A. Widely Tunable and Anisotropic Charge Carrier Mobility in Monolayer Tin(Ii) Selenide Using Biaxial Strain: A First-Principles Study. *J. Mater. Chem. C* **2017**, *5* (5), 1247−1254.

(19) Wang, K.; Kuo, T.-W.; Yang, T.-Y.; Cyu, R.-H.; Hsu, C.-W.; Hsu, Y.-C.; Yu, Y.-J.; Chen, Y.-Z.; Chueh, Y.-L. Controllable Oxygen-Incorporated 2D-SnSe2 Layered Thin Film by Plasma-Assisted Selenization Process with Enhanced NO2 Gas Sensitivity and Improved Humidity Stability. *Adv. Mater. Technol.* **2024**, *9* (2), 2301507.

(20) Hsu, C.-H.; Liao, H.-Y.; Wang, K.; Kuo, T.-W.; Liu, C.-C.; Shih, J.-R.; Lin, C.-J.; Chen, C.-T.; Peng, Y.-R.; Yang, T.-Y.; Kao, M.-Y.; Huang, H.-F.; Shen, H.-Y.; King, Y.-C.; Chueh, Y.-L. Design of Wireless Multiple Gases Complementary Architecture Sensors Based on SnSe2 and PtSe2 Layered Films and Oscillating Circuits. *Adv. Mater. Technol.* **2024**, *9* (8), 2301479.

(21) El-Mahalawy, A. M.; Mansour, S. A.; Wassel, A. R.; Mohamed, A. E.; Ali, S. E. Impact of Structural and Optical Properties Tunability of SnSe2 Thin Films on Its Optoelectronic Properties. *Surf. Interfaces* **2022**, *33*, 102251.

(22) Gupta, S. U.; Dalvaniya, A. G.; Chauhan, P.; Patel, K. D.; Solanki, G. K.; Pathak, V. M.; Jha, P. K. Cryotronic Low-Powered Strained Polymorphic Photodetector Functionalized by Palladium Incorporated Tin Diselenide. *Adv. Opt. Mater.* **2022**, *10* (20), 2201302.
(23) Gupta, S. U.; Dalvaniya, A. G.; Patel, N. F.; Bhakhar, S. A.; Nair, S.; Joy, J.; Patel, K. D.; Solanki, G. K.; Pathak, V. M.; Som, N. N.; Jha, P. K.; Panda, D. K. Optical Switching Device Based on a Crystalline SnSe2 Photodetector in Diverse Conditions. *ACS Appl. Electron. Mater.* **2021**, *3* (11), 4859−4869.
(24) Mukhokosi, E. P.; Roul, B.; Krupanidhi, S. B.; Nanda, K. K. Toward a Fast and Highly Responsive SnSe 2-Based Photodiode by Exploiting the Mobility of the Counter Semiconductor. *ACS Appl. Mater. Interfaces* **2019**, *11*, 6184.
(25) Zhou, X.; Gan, L.; Tian, W.; Zhang, Q.; Jin, S.; Li, H.; Bando, Y.; Golberg, D.; Zhai, T. Ultrathin SnSe2 Flakes Grown by Chemical Vapor Deposition for High-Performance Photodetectors. *Adv. Mater.* **2015**, *27* (48), 8035−8041.
(26) Bougouma, M.; Batan, A.; Guel, B.; Segato, T.; Legma, J.; Reniers, F.; Delplancke-Ogletree, M. P.; Buess-Herman, C.; Doneux, T. Growth and Characterization of Large, High Quality MoSe2 Single Crystals. *J. Cryst. Growth* **2013**, *363*, 122−127.
(27) Dixit, V.; Nair, S.; Joy, J.; Vyas, C. U.; Patel, A. B.; Chauhan, P.; Sumesh, C. K.; Narayan, S.; Jha, P. K.; Solanki, G. K.; Patel, K. D.; Pathak, V. M. Growth and Application of WSe2 Single Crystal Synthesized by DVT in Thin Film Hetero-Junction Photodetector. *Eur. Phys. J. B* **2019**, *92* (6), 118.
(28) Gupta, S. U.; Dalvaniya, A. G.; Limberkar, C.; Patel, K. D.; Solanki, G. K.; Pathak, V. M.; Pataniya, P. M.; Sumesh, C. K.; Som, N. N.; Jha, P. K.; Patel, V. Annealing Induced Phase Transformation from Amorphous to Polycrystalline SnSe2 Thin Film Photo Detector with Enhanced Light-Matter Interaction. *J. Non-Cryst. Solids* **2022**, *578*, 121353.
(29) Yu, J.; Xu, C.-Y.; Li, Y.; Zhou, F.; Chen, X.-S.; Hu, P.-A.; Zhen, L. Ternary SnS2-XSex Alloys Nanosheets and Nanosheet Assemblies with Tunable Chemical Compositions and Band Gaps for Photodetector Applications. *Sci. Rep.* **2015**, *5* (1), 17109.
(30) Chauhan, P.; Patel, A. B.; Solanki, G. K.; Patel, K. D.; Pathak, V. M.; Sumesh, C. K.; Narayan, S.; Jha, P. K. Rhenium Substitutional Doping for Enhanced Photoresponse of N-SnSe2/p-Si Heterojunction Based Tunable and High-Performance Visible-Light Photodetector. *Appl. Surf. Sci.* **2021**, *536*, 147739.
(31) Zankat, C. K.; Pataniya, P.; Tannarana, M.; Solanki, G. K.; Patel, K. D.; Pathak, V. M. High Performance Humidity Sensor Based on V0.5Sn0.5Se2 Ternary Alloy. *J. Mater. Sci.: Mater. Electron.* **2019**, *30* (6), 6065−6070.
(32) Wu, S.; Yang, H.; Wu, Z.; Liu, C.; Miao, L.; Gao, J.; Wang, X.; Wang, X.; Shen, C.; Noudem, J. G.; Wang, J. Enhancement of Thermoelectric Performance of Layered SnSe2 by Synergistic Modulation of Carrier Concentration and Suppression of Lattice Thermal Conductivity. *ACS Appl. Energy Mater.* **2019**, *2* (12), 8481−8490.
(33) Wu, J.; Hu, Z.; Jin, Z.; Lei, S.; Guo, H.; Chatterjee, K.; Zhang, J.; Yang, Y.; Li, B.; Liu, Y.; Lai, J.; Vajtai, R.; Yakobson, B.; Tang, M.; Lou, J.; Ajayan, P. M. Spiral Growth of SnSe2 Crystals by Chemical Vapor Deposition. *Adv. Mater. Interfaces* **2016**, *3* (16), 1600383.
(34) Wang, J.; Huang, J.; Li, Y.; Ding, K.; Jiang, D.; Dou, X.; Sun, B. Radiative and Non-Radiative Exciton Recombination Processes in a Chemical Vapor Deposition-Grown MoSe2Film. *J. Phys. Chem. C* **2022**, *126* (36), 15319−15326.
(35) Zhang, Q.; Li, M.; Lochocki, E. B.; Vishwanath, S.; Liu, X.; Yan, R.; Lien, H. H.; Dobrowolska, M.; Furdyna, J.; Shen, K. M.; Cheng, G.; Hight Walker, A. R.; Gundlach, D. J.; Xing, H. G.; Nguyen, N. V. Band Offset and Electron Affinity of MBE-Grown SnSe2. *Appl. Phys. Lett.* **2018**, *112* (4), 042108.
(36) Kandar, S.; Bhatt, K.; Kapoor, A.; Singh, R. Stacking-Order Independent Inter-Layer Charge Transfer in MBE-Grown MoSe2 and WSe2 Heterostructures. *Surf. Interfaces* **2024**, *55*, 105446.
(37) Chen, W.; Hu, M.; Zong, J.; Xie, X.; Meng, Q.; Yu, F.; Wang, L.; Ren, W.; Chen, A.; Liu, G.; Xi, X.; Li, F.-S.; Sun, J.; Liu, J.; Zhang, Y. Epitaxial Growth of Single-Phase 1T'-WSe2Monolayer with Assistance of Enhanced Interface Interaction. *Adv. Mater.* **2021**, *33* (7), 2004930.
(38) Lee, S.; Truong, L.; Lee, M.-J.; Chun, S.-H. Comparative Study of SnSe2 Exfoliation and the Photothermal Current from the Products. *Cryst. Growth Des.* **2021**, *21* (12), 6648−6654.
(39) Strauß, F.; Kohlschreiber, P.; Keck, J.; Michel, P.; Hiller, J.; Meixner, A. J.; Scheele, M. A Simple 230 MHz Photodetector Based on Exfoliated WSe2Multilayers. *RSC Appl. Interfaces* **2024**, *1* (4), 728−733.
(40) Zhang, Y.; Zhai, Y.; Li, J.; Fang, W. The Improvement of the Mechanical Exfoliation Method to Prepare Impurity-Free Few-Layer MoS2. In *2023 IEEE International Conference on Manipulation, Manufacturing and Measurement on the Nanoscale (3M-NANO)*; 2023; pp 477−481.
(41) Shi, J.; Chen, X.; Zhao, L.; Gong, Y.; Hong, M.; Huan, Y.; Zhang, Z.; Yang, P.; Li, Y.; Zhang, Q.; Zhang, Q.; Gu, L.; Chen, H.; Wang, J.; Deng, S.; Xu, N.; Zhang, Y. Chemical Vapor Deposition Grown Wafer-Scale 2D Tantalum Diselenide with Robust Charge-Density-Wave Order. *Adv. Mater.* **2018**, *30* (44), 1804616.
(42) Shao, X.; Li, S.; Tang, D. M. Flaky Nano-Crystalline SnSe2 Thin Films for Photoelectrochemical Current Generation. *RSC Adv.* **2018**, *8* (56), 32157−32163.
(43) Patel, M.; Bhakhar, S.; Solanki, G. K. Showcasing a Self-Powered Photoelectrochemical Photodetector with Ultrasonically Exfoliated SnSe2 Nanosheets. *J. Mater. Sci.: Mater. Electron.* **2024**, *35* (8), 550.
(44) Zappia, M. I.; Bianca, G.; Bellani, S.; Serri, M.; Najafi, L.; Oropesa-Nuñez, R.; Martín-García, B.; Bouša, D.; Sedmidubský, D.; Pellegrini, V.; Sofer, Z.; Cupolillo, A.; Bonaccorso, F. Solution-Processed GaSe Nanoflake-Based Films for Photoelectrochemical Water Splitting and Photoelectrochemical-Type Photodetectors. *Adv. Funct. Mater.* **2020**, *30* (10), 1909572.
(45) Voudoukis, N.; Oikonomidis, S. Inverse Square Law for Light and Radiation: A Unifying Educational Approach. *Eur. J. Eng. Technol. Res.* **2017**, *2*, 23−27.
(46) Gonzalez, J. M.; Oleynik, I. I. Layer-Dependent Properties of SnS2 and SnSe2 Two-Dimensional Materials. *Phys. Rev. B* **2016**, *94* (12), 125443.
(47) Mukhokosi, E. P.; Krupanidhi, S. B.; Nanda, K. K. Band Gap Engineering of Hexagonal SnSe2 Nanostructured Thin Films for Infra-Red Photodetection. *Sci. Rep.* **2017**, *7* (1), 15215.
(48) Lu, D.; Yue, C.; Luo, S.; Li, Z.; Xue, W.; Qi, X.; Zhong, J. Phase Controllable Synthesis of SnSe and SnSe2 Films with Tunable Photoresponse Properties. *Appl. Surf. Sci.* **2021**, *541*, 148615.
(49) Lu, C.; Dong, W.; Zou, Y.; Wang, Z.; Tan, J.; Bai, X.; Ma, N.; Ge, Y.; Zhao, Q.; Xu, X. Direct Z-Scheme SnSe2/SnSe Heterostructure Passivated by Al2O3 for Highly Stable and Sensitive Photoelectrochemical Photodetectors. *ACS Appl. Mater. Interfaces* **2023**, *15* (4), 6156−6168.
(50) Xue, X.; Lu, C.; Luo, M.; Han, T.; Liu, Y.; Ge, Y.; Dong, W.; Xu, X. Type-I SnSe2/ZnS Heterostructure Improving Photoelectrochemical Photodetection and Water Splitting. *Sci. China Mater.* **2023**, *66* (1), 127−138.
(51) Yang, J. K.; Liang, B.; Zhao, M. J.; Gao, Y.; Zhang, F. C.; Zhao, H. L. Reference of Temperature and Time during Tempering Process for Non-Stoichiometric FTO Films. *Sci. Rep.* **2015**, *5* (1), 15001.
(52) Korjenic, A.; Raja, K. S. Electrochemical Stability of Fluorine Doped Tin Oxide (FTO) Coating at Different PH Conditions. *J. Electrochem. Soc.* **2019**, *166* (6), C169.
(53) Wang, X.; Ding, K.; Huang, L.; Li, X.; Ye, L.; Luo, J.; Jiang, J.; Li, H.; Xiong, Y.; Ye, L.; Pang, D.; Tang, Y.; Li, W.; Zhang, H.; Kong, C. Enhancing the Performance of Self-Powered Deep-Ultraviolet Photoelectrochemical Photodetectors by Constructing α-Ga2O3@a-Al2O3 Core-Shell Nanorod Arrays for Solar-Blind Imaging. *Appl. Surf. Sci.* **2024**, *648*, 159022.


https://doi.org/10.1021/acssuschemeng.5c03239
ACS Sustainable Chem. Eng. 2025, 13, 12010−12021

(54) Luo, Y.; Wang, D.; Kang, Y.; Liu, X.; Fang, S.; Memon, M. H.; Yu, H.; Zhang, H.; Luo, D.; Sun, X.; Ooi, B. S.; Gong, C.; Xu, Z.; Sun, H. Demonstration of Photoelectrochemical-Type Photodetectors Using Seawater as Electrolyte for Portable and Wireless Optical Communication. *Adv. Opt. Mater.* **2022**, *10* (10), 2102839.
(55) Khatun, S.; Hirani, H.; Roy, P. Seawater Electrocatalysis: Activity and Selectivity. *J. Mater. Chem. A* **2021**, *9*, 74−86.
(56) Ding, K.; Zhang, H.; Jiang, J.; Luo, J.; Wu, R.; Ye, L.; Tang, Y.; Pang, D.; Li, H.; Li, W. Balancing Carrier Dynamics in Oxygen-Vacancy-Tuned Amorphous Ga2O3 Thin-Film Self-Powered Photoelectrochemical-Type Solar-Blind Photodetector Arrays for Underwater Imaging. *Advanced Science* **2024**, *11* (43), 2407822.
(57) Liu, X.; Wang, D.; Shao, P.; Sun, H.; Fang, S.; Kang, Y.; Liang, K.; Jia, H.; Luo, Y.; Xue, J.; Wang, J.; Zhi, T.; Chen, D.; Liu, B.; Long, S.; Zhang, R. Achieving Record High External Quantum Efficiency > 86.7% in Solar-Blind Photoelectrochemical Photodetection. *Adv. Funct. Mater.* **2022**, *32* (28), 2201604.
(58) Mayer, M. T.; Du, C.; Wang, D. Hematite/Si Nanowire Dual-Absorber System for Photoelectrochemical Water Splitting at Low Applied Potentials. *J. Am. Chem. Soc.* **2012**, *134* (30), 12406−12409.
(59) Zhao, G.; Sun, Z.; Mei, B. Oxygen Vacancies Modified Bi4O5I2 for Sensitive and Stable Photoelectrochemical-Type Photodetection. *Adv. Opt. Mater.* **2024**, *12* (6), 2302029.
(60) Li, J.; Griep, M.; Choi, Y.; Chu, D. Photoelectrochemical Overall Water Splitting with Textured CuBi2O4 as a Photocathode. *Chem. Commun.* **2018**, *54* (27), 3331−3334.
(61) Zhang, Z.; Ji, P.; Li, S.; Wang, F.; He, S.; Cheng, Y.; Zhao, S.; Li, K.; Wang, X.; Wang, Y.; Yang, S. High-Performance Broadband Flexible Photodetector Based on Gd3Fe5O12-Assisted Double van Der Waals Heterojunctions. *Microsyst. Nanoeng.* **2023**, *9* (1), 84.
(62) Gupta, S. U.; Gour, N. I.; Dalvaniya, A. G.; Solanki, D. G.; Patel, J. Ka.; Vyas, P. D.; Bhakhar, S. A.; Chauhan, B. L.; Patel, K. D.; Solanki, G. K.; Patel, M.; Sumesh, C. K.; Jha, P. K.; Patel, V. Alloy Engineered Cryotronically Stable Polymorphic Strained Photo Detector Functionalized by Palladium Enriched Tin Diselenide Nanosheets. *J. Alloys Compd.* **2024**, *1005*, 176128.
(63) Zhang, N.; Lin, Z.; Wang, Z.; Zhu, S.; Chen, D.; Qi, H.; Zheng, W. Under-Seawater Immersion $\beta$-Ga2O3 Solar-Blind Ultraviolet Imaging Photodetector with High Photo-to-Dark Current Ratio and Fast Response. *ACS Nano* **2024**, *18* (1), 652−661.
(64) Yu, C.; Li, H.; Ding, K.; Huang, L.; Zhang, H.; Pang, D.; Xiong, Y.; Yang, P.-A.; Fang, L.; Li, W.; Tang, Y.; Ye, L.; Kong, C. Flexible and Self-Powered Photoelectrochemical-Type Solar-Blind Photodetectors Based on Ag Nanowires-Embedded Amorphous Ga2O3 Films. *Adv. Opt. Mater.* **2024**, *12* (18), 2400116.
(65) Cheng, F.; Feng, X.; Chen, X.; Lin, W.; Rong, J.; Yang, W. Synergistic Action of Co-Fe Layered Double Hydroxide Electrocatalyst and Multiple Ions of Sea Salt for Efficient Seawater Oxidation at near-Neutral PH. *Electrochim. Acta* **2017**, *251*, 336−343.
(66) Zhang, J.; Jiang, M.; Zhou, M.; Yang, W.; Zhao, Y.; Lu, S. Self-Powered (In,Ga)N-Nanowire-Based Photodetector with Fast Response Speed for under-Seawater Detection. *Opt. Express* **2023**, *31* (5), 8128−8138.
(67) Li, Y.; Zhou, H.; Cai, S.; Prabhakaran, D.; Niu, W.; Large, A.; Held, G.; Taylor, R. A.; Wu, X.-P.; Tsang, S. C. E. Electrolyte-Assisted Polarization Leading to Enhanced Charge Separation and Solar-to-Hydrogen Conversion Efficiency of Seawater Splitting. *Nat. Catal.* **2024**, *7* (1), 77−88.
(68) Iguchi, S.; Teramura, K.; Hosokawa, S.; Tanaka, T. Effect of the Chloride Ion as a Hole Scavenger on the Photocatalytic Conversion of CO2 in an Aqueous Solution over Ni-Al Layered Double Hydroxides. *Phys. Chem. Chem. Phys.* **2015**, *17* (27), 17995−18003.
(69) Ma, Q.; Yan, C.; Lv, W.; Mei, Y.; Peng, H.; Du, J.; Zheng, B.; Guo, Y. Coexisting Chloride Ion for Boosting the Photoelectrocatalytic Degradation Efficiency of Organic Dyes. *Catal. Lett.* **2023**, *153* (2), 378−387.
(70) Li, Z.; Qiao, H.; Guo, Z.; Ren, X.; Huang, Z.; Qi, X.; Dhanabalan, S. C.; Ponraj, J. S.; Zhang, D.; Li, J.; Zhao, J.; Zhong, J.; Zhang, H. High-Performance Photo-Electrochemical Photodetector Based on Liquid-Exfoliated Few-Layered InSe Nanosheets with Enhanced Stability. *Adv. Funct. Mater.* **2018**, *28* (16), 1705237.
(71) Xu, X.; Bai, X.; Han, T.; Dong, W.; Zhang, Y.; Wang, Y.; Lu, C.; Hua, D. High Performance UV-Vis Photodetectors Based on Tin Monosulfide Film Synthesized by Physical Vapor Deposition. *Appl. Surf. Sci.* **2022**, *597*, 153691.
(72) Wang, L.; Qin, M.; Kuklin, A. V.; Li, J.; Zhao, Y.; Zhang, J.; Ai, J.; Chen, Z.; Zhang, H.; Ågren, H.; Gao, L. Broad-Band Photoelectrochemical Photodetector Based on Ternary Sb2Te2Se Nanosheets. *Adv. Opt. Mater.* **2024**, *12*, 2401649.
(73) Gao, L.; Ma, C.; Wei, S.; Kuklin, A. V.; Zhang, H.; Ågren, H. Applications of Few-Layer Nb2C MXene: Narrow-Band Photodetectors and Femtosecond Mode-Locked Fiber Lasers. *ACS Nano* **2021**, *15* (1), 954−965.




https://doi.org/10.1021/acssuschemeng.5c03239
ACS Sustainable Chem. Eng. 2025, 13, 12010−12021